

# Revisiting Solvent Additives for the Fabrication of Polymer:Fullerene Solar Cells: Exploring a Series of Benzaldehydes

Christian Sprau, Jens Kattenbusch, Yonghe Li, Erich Müller, Dagmar Gerthsen, Rüdiger Berger, Jasper J. Michels, and Alexander Colsmann\*

The power conversion efficiencies of organic solar cells delicately depend on the morphology of the light-harvesting bulk heterojunctions (BHJ). Upon deposition from solution, the formation of tailored bicontinuous networks of polymers and fullerenes is often achieved using combinations of solvents and solvent additives. Common wisdom infers that best solar cell performances are achieved when the solvent additives exhibit excellent fullerene solubility. Herein, this concept is revisited based on the investigation of a series of structurally similar, substituted benzaldehydes. It is concluded that the solvent additives do not only have to feature the commonly accepted good fullerene solubility, but must also exhibit lowest polymer solubility to suppress liquid–liquid demixing and hence achieve best solar cell performance. Thus, this study adds an important item to the list of selection criteria of solvent additives toward the production of polymer:fullerene solar cells with optimized power conversion efficiencies. The microscopic picture of the resulting domain configurations within the light-harvesting layers is developed around comprehensive multiscale investigations of the BHJ morphology, using atomic force microscopy, scanning transmission electron microscopy, and nano-infrared microscopy. The latter is operated in two complementary modes, one of which is more bulk sensitive, whereas the other mode is surface sensitive.

## 1. Introduction

The unique features of organic solar cells, such as semitransparency, freedom in color and design, mechanical flexibility and roll-to-roll printability on large scale, are important enablers for novel solar energy applications such as integration into windows or façade elements, mobile applications or self-powered sensors


for the internet of things.<sup>[1–4]</sup> Over the past decade, tremendous efforts on both the synthesis of novel light-harvesting semiconductors and the optimization of deposition processes have steadily increased the power conversion efficiency (PCE) of solution-processed polymer solar cells, recently exceeding 17%.<sup>[5–8]</sup>

The light-harvesting bulk heterojunctions (BHJs) in organic solar cells comprise blends of (at least) two semiconductors, an electron donor and an electron acceptor. Photogenerated excitons are dissociated at the interface of the two material phases by transition of one of the two bound charge carriers to the other semiconductor species. While the short exciton lifetime requires an intimately mixed BHJ for fast exciton dissociation, the charge carrier transport to the electrodes calls for well-crafted bicontinuous pathways. Thus, highest PCEs are only achieved if the two semiconductors within the BHJ are well organized. Archetypal organic solar cells comprise blends of donor polymers and acceptor fullerenes, whereas more modern device concepts use non-

fullerene acceptors (NFAs) for better absorption coverage of the solar spectrum. Yet, the synthesis of today's NFAs follows a rather laborious route with many steps and low yields,<sup>[9]</sup> which is why fullerenes are still the acceptors of choice for industrial process implementation.

When deposited from solution, the BHJ formation process during the drying of the thin-film must be well designed.

C. Sprau, Y. Li, E. Müller, D. Gerthsen, A. Colsmann  
Material Research Center for Energy Systems (MZE)  
Karlsruhe Institute of Technology (KIT)  
Strasse am Forum 7, 76131 Karlsruhe, Germany  
E-mail: alexander.colsmann@kit.edu

 The ORCID identification number(s) for the author(s) of this article can be found under <https://doi.org/10.1002/solr.202100238>.

© 2021 The Authors. Solar RRL published by Wiley-VCH GmbH. This is an open access article under the terms of the Creative Commons Attribution License, which permits use, distribution and reproduction in any medium, provided the original work is properly cited.

DOI: 10.1002/solr.202100238

C. Sprau, J. Kattenbusch, A. Colsmann  
Light Technology Institute (LTI)  
Karlsruhe Institute of Technology (KIT)  
Engesserstrasse 13, 76131 Karlsruhe, Germany

Y. Li, E. Müller, D. Gerthsen  
Laboratory for Electron Microscopy (LEM)  
Karlsruhe Institute of Technology (KIT)  
Engesserstr. 7, 76131 Karlsruhe, Germany

R. Berger, J. J. Michels  
Max Planck Institute for Polymer Research  
Ackermannweg 10, 55128 Mainz, Germany

Blends that inherently tend to mix too intimately, e.g., poly[3-hexylthiophene-2,5-diyl] (P3HT) and [6,6]-phenyl-C<sub>61</sub>-butyric acid methyl ester (PC<sub>61</sub>BM),<sup>[10–13]</sup> can be controlled to phase separate to a certain degree by slow-drying under vapor atmosphere or by thermal postprocessing. Others, such as blends of diketopyrrolopyrrole polymers and fullerenes,<sup>[14]</sup> commonly show strong macro-phase separation, usually via spinodal decomposition in the liquid state. Further examples are reviewed in the Supporting Information. In these cases, thermal or solvent-vapor annealing is not useful and may even drive further phase separation. For a more intimate semiconductor mixture, the BHJ formation in such blends can be controlled with small amounts (typically 3 vol%) of certain solvent additives, such as 1,8-diiodooctane (DIO).<sup>[15–18]</sup>

While common lab solvents such as 1,2-dichlorobenzene or chloroform sometimes produce rather good polymer:fullerene BHJ morphologies, industry standards require less toxic and less environmental harmful solvents. If nonchlorinated solvents are used, such as *o*-xylene, many polymer:fullerene combinations undergo strong macro-phase separation by liquid–liquid (L–L) demixing during BHJ formation which leads to the formation of a dispersed, lens-shaped fullerene phase with domain sizes of up to several hundred nanometers.<sup>[19,20]</sup> These comparably large fullerene domains cause different local charge carrier generation and extraction efficiencies,<sup>[21]</sup> and geminate and nongeminate recombination account for a substantially lower PCE than in optimized blends.<sup>[22]</sup> This formation of large fullerene domains is not specific to blends comprising a certain type of polymer, but was observed for diketopyrrolopyrrole,<sup>[14,23]</sup> dithienogermole-thienopyrrolodione or dithienosilole-thienopyrrolodione,<sup>[16]</sup> benzodithiophene-benzotriazole,<sup>[24]</sup> benzodithiophene-quinoxaline<sup>[19]</sup> and, most prominently, benzodithiophene-thienothiophene<sup>[25,26]</sup> polymers such as poly[4,8-bis[(2-ethylhexyl)oxy]benzo[1,2-b:4,5-b']dithiophene-2,6-diyl][3-fluoro-2-[(2-ethylhexyl)carbonyl]thieno[3,4-b]thiophenediyl]] (PTB7).<sup>[15,17,27]</sup> If strong macro-phase separation occurs, e.g., upon processing from less toxic solvents, the use of solvent additives will become crucially important. Apart from the omnipresent DIO, the application of other solvent additives, such as 1-chloronaphthalene (CN),<sup>[28,29]</sup> 1,8-octanedithiol (ODT),<sup>[30]</sup> or diphenyl ether (DPE),<sup>[31,32]</sup> has been reported in the literature.

It has been widely agreed upon that the solubility of the semiconductors in the solvent additive plays a key role in the identification of suitable solvent additives. Today's criteria to choose solvent additives date back to the work by Lee et al., in 2008. In

their very first studies employing solvent additives in organic solar cells, ODT<sup>[30]</sup> (and later DIO)<sup>[33]</sup> fostered the aggregation of the polymer in a blend of a cyclopentadithiophene–benzothiadiazole polymer (PCPDTBT) and [6,6]-phenyl-C<sub>71</sub>-butyric acid methyl ester (PC<sub>71</sub>BM), and thus promoted nanoscale phase separation. According to these observations on too intimately mixed PCPDTBT:PC<sub>71</sub>BM, Lee et al. proposed guidelines for suitable solvent additives: 1) the solvent additive must exhibit selective (differential) solubility of the fullerene, and 2) the solvent additive must have a higher boiling point than the main solvent to become effective when the main solvent has evaporated.<sup>[33]</sup> Even though these guidelines have been developed for too intimately mixing blends, they are also used for blends that exhibit strong macro-phase separation by L–L demixing.

Yet, to date, the applicability or nonapplicability of Lee's rules to phase separating blends remains to be proven, and controversial conclusions in the literature call for a review of the guidelines: For example, the solvent additives ODT and CN were used to produce P3HT:PC<sub>61</sub>BM solar cells with good performance through promoting the aggregation of P3HT in an otherwise too intimately mixed BHJ. While both P3HT and PC<sub>61</sub>BM are well soluble in CN,<sup>[29]</sup> ODT is typically a poor solvent for aromatic polymers but a good solvent for fullerenes, i.e., it exhibits selective solubility to the fullerene.<sup>[33]</sup> Even though these additives produce solar cells with similar PCE, a detailed analysis of the morphology formation by in situ X-ray methods revealed different working mechanisms:<sup>[34,35]</sup> ODT separated the liquid amorphous phases and fostered P3HT crystallization in the fullerene-depleted phase, whereas CN promoted polymer crystallization in a CN-plasticized amorphous P3HT:PC<sub>61</sub>BM mixed phase due to prolonged drying times.

Recent trends in the organic photovoltaic community to replace the commonly used hazardous halogenated solvents by more eco-friendly, non-halogenated solvents,<sup>[20,36–38]</sup> also fostered the need of alternative non-halogenated and ecofriendly solvent additives and their selection rules.

Previously, we have shown that the ecofriendly *p*-anisaldehyde can replace the hazardous DIO in the formation process of PTB7:PC<sub>71</sub>BM and several other high-performance polymer:fullerene blends.<sup>[39,40]</sup> In this work, we investigate a series of structurally similar, substituted benzaldehydes as solvent additives, i.e., benzaldehyde (BA), *p*-tolualdehyde (TA), *m*-salicylaldehyde (SA), and *p*-anisaldehyde (AA) (Figure 1). We propose more generalized criteria to identify solvent additives which are suitable to

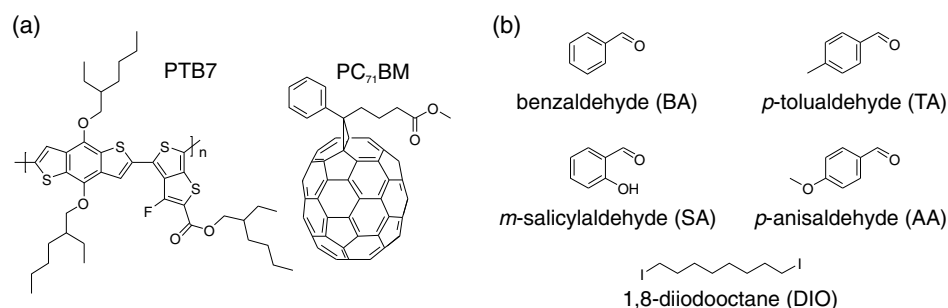


**Figure 1.** Chemical structures of a) the light-harvesting organic semiconductors PTB7 and PC<sub>71</sub>BM and b) the benzaldehyde solvent additives investigated in this work.

suppress or control phase separation within the polymer:fullerene BHJ to produce organic solar cells with optimized PCEs. The effect of the solvent additives on the formation of a PTB7:PC<sub>71</sub>BM BHJ is studied by correlating photovoltaic performance with the thin-film morphology, which is investigated by atomic force microscopy (AFM), nano-infrared force microscopy (nano-IR), and scanning transmission electron microscopy (STEM), as well as by quantifying the semiconductor solubility.

## 2. Solar Cell Performance

To investigate the effect of the series of benzaldehyde solvent additives on the device performance, we fabricated organic solar cells with an inverted indium tin oxide (ITO)/ZnO/PTB7:PC<sub>71</sub>BM/MoO<sub>x</sub>/Ag device architecture. Initially, we spin cast the light-harvesting PTB7:PC<sub>71</sub>BM layer from neat *o*-xylene which is one of the most often used non-halogenated and industrially relevant solvents. The devices exhibited a poor average fill factor (FF) = 40% and a short-circuit current density ( $J_{SC}$ ) < 6 mA cm<sup>-2</sup> at an open-circuit voltage ( $V_{OC}$ ) = 0.74 V, resulting in a PCE of 1.7%. Notably, single solvent casting from other main solvents, such as chlorobenzene or anisole, produced similar results.<sup>[39]</sup> Then we repeated the experiments employing either of the solvent additives BA, TA, SA, AA, and, for reference, DIO at different concentrations. The concentration of all solvent additives was optimized separately for best solar cell performance. **Figure 2** shows the current density–voltage ( $J$ – $V$ ) characteristics of representative solar cells and displays the dependence of the key parameters PCE, FF,  $J_{SC}$ , and  $V_{OC}$  on the solvent additive amount. The solvent additive was added in relation to the main solvent volume and ranged from 0% to 10%. The key parameters are also shown in **Table 1**. The full set of  $J$ – $V$  curves for all solvent additive-to-solvent ratios is included in Figure S1, Supporting Information.

Upon addition of DIO to the main solvent *o*-xylene, the best PTB7:PC<sub>71</sub>BM solar cell PCE = 6.6% was achieved at a concentration of 3%. Higher DIO amounts of up to 10% slightly reduced the PCE which is well in line with previous studies.<sup>[25,41]</sup> While DIO is arguably one of the most often used and best investigated solvent additives, it is classified hazardous and its very high boiling point as well as its slow and often incomplete evaporation from the light-harvesting layers hamper its use in high-throughput solar cell fabrication. Here, benzaldehydes can present a case as being ecofriendly and exhibiting much better drying properties.<sup>[39]</sup>

Among the series of benzaldehydes, we found two groups with different effects on the BHJ formation. Upon addition of 10% BA to the *o*-xylene solution of PTB7:PC<sub>71</sub>BM, the PCE of the corresponding (optimized) organic solar cells improved only marginally to 2.7% versus the use of neat *o*-xylene. This improvement originated from a minor increase of the FF to 45% and of the  $J_{SC}$  to 7.8 mA cm<sup>-2</sup>, but the performance still remained significantly below the PCE = 7% that can be expected for optimized PTB7:PC<sub>71</sub>BM solar cells. Similarly, using 0.5% of TA as the solvent additive, the best achievable PCE was only 2.2%, further decreasing toward higher TA amounts. As such, neither the addition of BA nor TA to the *o*-xylene solution produced competitive solar cells.

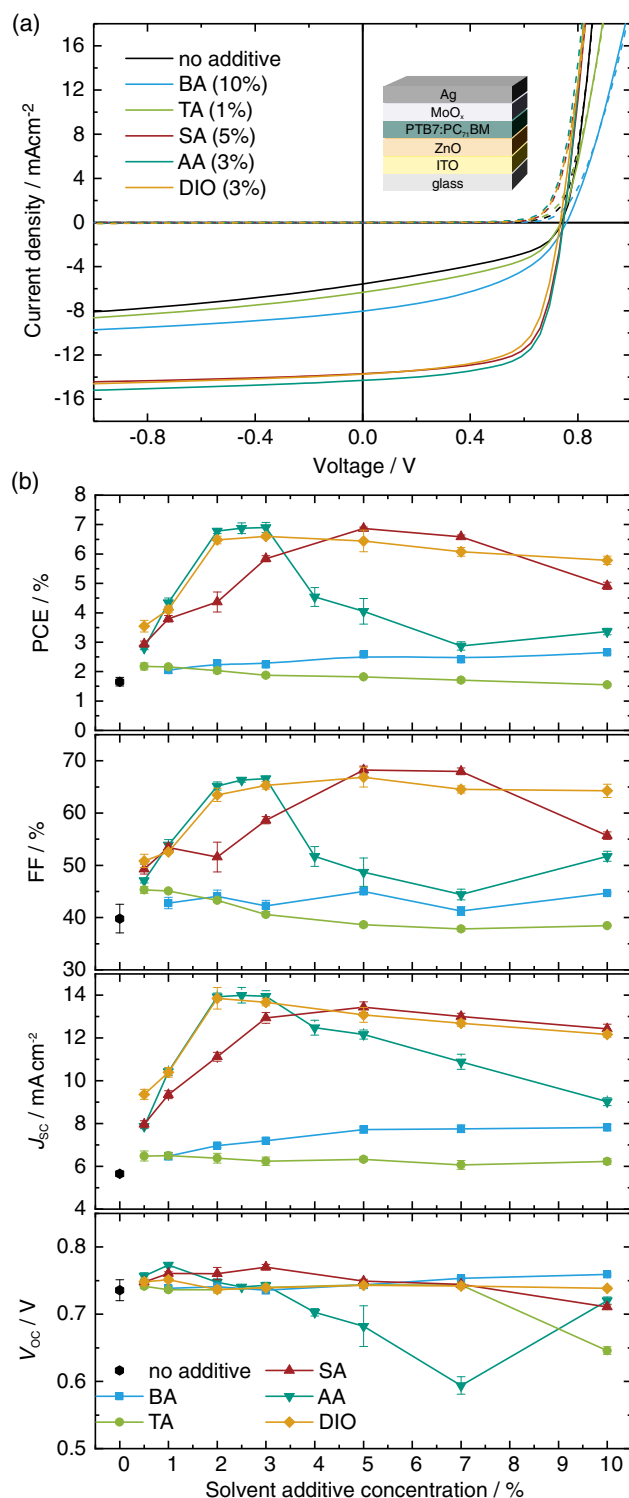


**Figure 2.** a) Representative  $J$ – $V$  curves in the dark (dashed lines) and under 1 sun equivalent illumination (solid lines) of the solar cells comprising PTB7:PC<sub>71</sub>BM layers processed from neat *o*-xylene or from an *o*-xylene: additive combination at the individually optimized solvent additive concentration. The inset depicts the device architecture. b) Dependence of the averaged solar cell key parameters PCE, FF,  $J_{SC}$ , and  $V_{OC}$  on the solvent additive concentration. Error bars represent the standard deviation averaged over several devices. Solid lines serve as a guide to the eye only.

**Table 1.** Averaged key parameters of the solar cells comprising light-harvesting PTB7:PC<sub>71</sub>BM layers cast from *o*-xylene with different solvent additives and different solvent additive concentrations as well as the roughness  $R_q$  of the PTB7:PC<sub>71</sub>BM layers as derived from AFM measurement.

| Solvent additive | Amount [%] | $J_{SC}$ [mA cm <sup>-2</sup> ] | $V_{OC}$ [V] | FF [%] | PCE <sup>a)</sup> [%] | $R_q$ [nm] |
|------------------|------------|---------------------------------|--------------|--------|-----------------------|------------|
| No additive      |            | 5.7                             | 0.74         | 40     | 1.7 (1.8)             | 17         |
| BA               | 1          | 6.5                             | 0.74         | 43     | 2.0 (2.2)             | 13         |
|                  | 2          | 7.0                             | 0.74         | 44     | 2.3 (2.4)             | 13         |
|                  | 3          | 7.2                             | 0.74         | 42     | 2.2 (2.3)             | 13         |
|                  | 5          | 7.7                             | 0.74         | 45     | 2.6 (2.7)             | 14         |
|                  | 7          | 7.8                             | 0.75         | 41     | 2.4 (2.5)             | 21         |
|                  | 10         | 7.8                             | 0.76         | 45     | 2.7 (2.7)             | 32         |
| TA               | 0.5        | 6.5                             | 0.74         | 45     | 2.2 (2.3)             | 15         |
|                  | 1          | 6.5                             | 0.74         | 45     | 2.2 (2.2)             | 16         |
|                  | 2          | 6.4                             | 0.74         | 43     | 2.0 (2.2)             | 21         |
|                  | 3          | 6.2                             | 0.74         | 41     | 1.9 (2.0)             | 26         |
|                  | 5          | 6.3                             | 0.74         | 39     | 1.8 (1.9)             | 38         |
|                  | 7          | 6.1                             | 0.74         | 38     | 1.7 (1.8)             | 48         |
| SA               | 10         | 6.2                             | 0.65         | 38     | 1.5 (1.6)             | 46         |
|                  | 0.5        | 8.0                             | 0.75         | 49     | 2.9 (3.0)             | 9.1        |
|                  | 1          | 9.3                             | 0.76         | 53     | 3.8 (3.9)             | 5.3        |
|                  | 2          | 11.1                            | 0.76         | 52     | 4.4 (5.0)             | 2.7        |
|                  | 3          | 12.9                            | 0.77         | 59     | 5.8 (5.9)             | 2.3        |
|                  | 5          | 13.4                            | 0.75         | 68     | 6.9 (6.9)             | 1.7        |
| AA               | 7          | 13.0                            | 0.74         | 68     | 6.6 (6.7)             | 2.1        |
|                  | 10         | 12.4                            | 0.71         | 56     | 4.9 (5.1)             | 3.9        |
|                  | 0.5        | 7.9                             | 0.76         | 47     | 2.8 (2.9)             | 7.4        |
|                  | 1          | 10.4                            | 0.77         | 54     | 4.3 (4.6)             | 4.5        |
|                  | 2          | 13.9                            | 0.75         | 65     | 6.8 (7.0)             | 4.5        |
|                  | 3          | 13.9                            | 0.74         | 67     | 6.9 (7.2)             | 3.0        |
| DIO              | 5          | 12.2                            | 0.68         | 49     | 4.1 (4.5)             | 17         |
|                  | 7          | 10.9                            | 0.59         | 44     | 2.9 (3.1)             | 35         |
|                  | 10         | 9.0                             | 0.72         | 52     | 3.4 (3.5)             | 52         |
|                  | 0.5        | 9.4                             | 0.75         | 51     | 3.5 (3.7)             | 5.7        |
|                  | 1          | 10.4                            | 0.75         | 53     | 4.1 (4.3)             | 8.9        |
|                  | 2          | 13.9                            | 0.74         | 63     | 6.5 (6.7)             | 6.1        |
| DIO              | 3          | 13.7                            | 0.74         | 65     | 6.6 (6.7)             | 6.6        |
|                  | 5          | 13.1                            | 0.74         | 67     | 6.4 (6.8)             | 9.0        |
|                  | 7          | 12.7                            | 0.74         | 65     | 6.1 (6.3)             | 9.2        |
|                  | 10         | 12.2                            | 0.74         | 64     | 5.8 (5.9)             | 13.3       |

<sup>a)</sup>PCEs in parentheses represent hero devices.

A completely different observation was made for SA and AA. Upon addition of 5% SA, the  $J_{SC}$  and the FF improved to 13.4 mA cm<sup>-2</sup> and 68%, producing a maximum PCE of 6.9%. SA presented itself with a rather broad process window which is beneficial for best reproducibility: At 7% SA, the PCE still yielded 6.6%. Toward higher SA amounts of 10%, the PCE

dropped to 4.9%. A similar picture was observed upon using AA. In line with our own previous results,<sup>[39]</sup> at a concentration of 2–3% of AA, an equally high PCE of 7% is reached but with a somewhat narrower processing window. Toward higher AA concentrations of 5% or more,  $J_{SC}$  and FF substantially drop and the  $J$ - $V$  curves indicate some device shunting. And even the  $V_{OC}$  drops below 0.7 V, whereas, in all other devices, the  $V_{OC}$  is much less affected by the choice and amount of the solvent additive. We note that we made similar observations using other main solvents instead of *o*-xylene, such as chlorobenzene or anisole.

The shape of the  $J$ - $V$  curves, and in particular, the changes observed in  $J_{SC}$  and FF, hint at differences in the charge carrier generation and extraction, depending on the additives and their amounts used during the deposition of the BHJ. We discuss the most relevant loss mechanisms, i.e., field-dependent generation of free charge carriers and enhanced bimolecular recombination, in the Supporting Information, analyzing the  $J$ - $V$  curves in reverse direction (Figure S2, Supporting Information).

At this point, the lesson learned is that SA and AA are excellent solvent additives for best performing solar cells with FF > 65% and  $J_{SC}$  > 13 mA cm<sup>-2</sup>, leading to PCEs of about 7%, even outperforming the DIO reference. In contrast, neither BA nor TA significantly improved the solar cell performance over the deposition from neat *o*-xylene.

### 3. Morphology of the BHJ

The common purpose of using solvent additives is the optimization of the microstructure of BHJs for lossless exciton dissociation and charge carrier transport to the electrodes. To better understand the effect of BA, TA, SA, and AA on the energy conversion in organic solar cells, we carried out a holistic analysis of the morphology of the light-harvesting PTB7:PC<sub>71</sub>BM layers on different length scales and with different sensitivities by a combination of AFM, nano-IR, and STEM.

#### 3.1. Topography Analyzed by AFM

Even though AFM only provides access to the surface of the BHJ, it still revealed an important difference between the layers processed with the solvent additives SA, AA, and DIO and those processed with BA and TA. **Figure 3** shows representative topography images of PTB7:PC<sub>71</sub>BM thin-films deposited from *o*-xylene using the various solvent additives and solvent additive concentrations. In accordance with earlier literature reports,<sup>[15,17,27]</sup> we found large lens-shaped fullerene domains in PTB7:PC<sub>71</sub>BM layers that were cast from neat *o*-xylene. These large fullerene domains, which are known to hamper (proper) solar cell performance,<sup>[21,22]</sup> reveal themselves by average protrusions of 45 nm with diameters of about 400 nm, evenly distributed over the surface.

In case of a low concentration of the poor solvent additive BA, we observed a minor reduction in size of the fullerene domains (diameter and protrusion). Strikingly, toward higher BA concentrations the domain sizes increased, and in layers processed with more than 5% of BA, the features grew larger than in the layers processed from neat *o*-xylene. Notably, protruding fullerene domains were present whenever adding BA at any concentration.

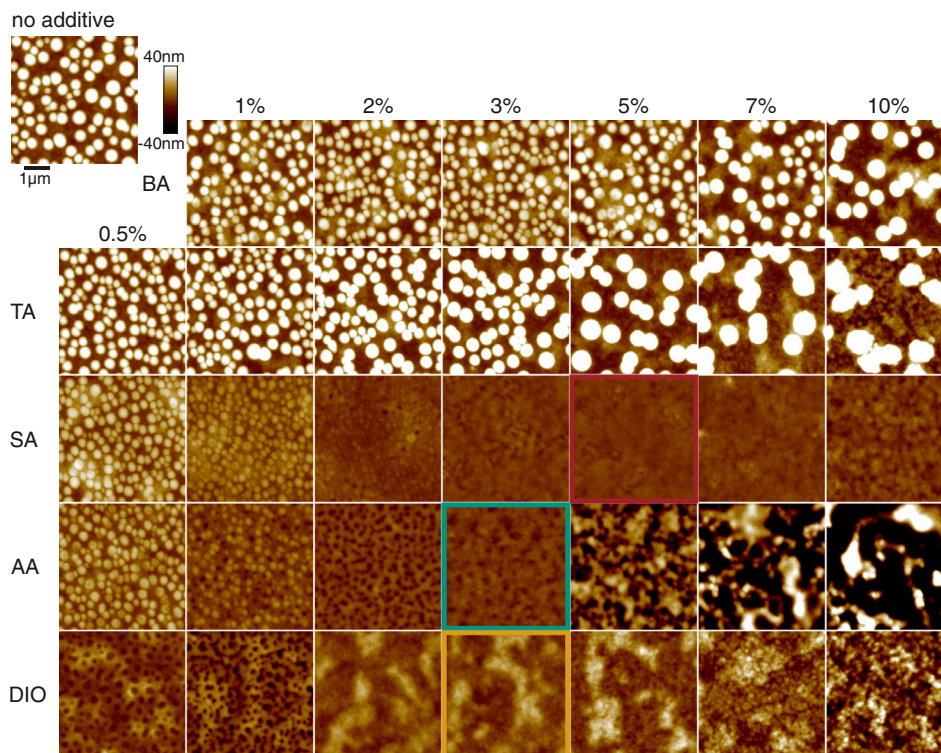


**Figure 3.** AFM topography of the PTB7:PC<sub>71</sub>BM layers cast from *o*-xylene using different solvent additives and solvent additive concentrations. Image size:  $5 \times 5 \mu\text{m}^2$ . Each row corresponds to one of the solvent additives (top to bottom: BA, TA, SA, AA, and DIO), whereas each column represents one solvent additive concentration (left to right: 0.5%, 1%, 2%, 3%, 5%, 7%, and 10%). For better comparison, all images deliberately use the same color scale, representing a topography range from  $-40$  to  $40$  nm, which results in some features exceeding this range and hence showing clipping. The respective optimum solvent additive concentrations that produced the highest solar cell PCEs are highlighted by a colored box.

Similarly, upon addition of TA to the solution, we observed the same features and witnessed the same growth of the fullerene domains towards higher TA concentrations. At a TA concentration of 10%, their diameter was on the order of  $1 \mu\text{m}$ , protruding  $150$  nm from the surface.

In contrast, we observed a reduction and eventual disappearance of the protruding fullerene domains upon using either of the good solvent additives SA, AA, or the reference additive DIO. When SA or AA was used, the lens-shaped fullerene domains were only visible in layers that were processed using smallest solvent additive concentrations, and even then, the dimensions of these features were significantly reduced compared with the additive-free, neat *o*-xylene case. Beyond 2% SA, the fullerene domains were no longer visible. In layers processed with 5% and 7% SA, the surface appeared smooth, with a root-mean-square roughness ( $R_q$ ) of only  $2$  nm. At these SA concentrations, the corresponding solar cells exhibited their maximum PCE =  $6.9\%$  (Figure 2). A higher SA concentration of 10% increased the surface roughness to  $4$  nm. Again, we witnessed the same effects and tendency in PTB7:PC<sub>71</sub>BM processed from *o*-xylene:AA solution. We only observed lens-shaped fullerene domains for low AA concentrations of 0.5% and 1%. At an AA concentration of 3%, where the solar cell performance was optimal, the protruding fullerene features vanished, and we found the smoothest and most homogeneous surface ( $R_q = 3$  nm). Toward higher AA concentrations, the surface became considerably rougher

( $R_q = 17, 35,$  and  $52$  nm at 5%, 7%, and 10%), where the peak-to-valley roughness exceeded the average film thickness ( $90$  nm) and thus explained the observed partial shunting of devices as discussed earlier.

Interestingly, the layers processed with 2% of AA are characterized by circular depressions with diameters of  $200$  nm (similar to the diameter of the protruding fullerene domains) and a depth of about  $15$  nm. Similarly, but more pronounced, we observed these depressions in layers cast with low DIO concentration (diameter:  $200$  nm; depth:  $8$  nm at 0.5% DIO,  $24$  nm at 1% DIO). We discuss these depressions in the Supporting Information and illustrate that, counterintuitively, these regions also correspond to fullerene-rich domains.

The full set of samples demonstrates that the larger the fullerene domains (or the larger the fullerene-rich depressions), the rougher is the surface. Thus, over all solvent additives and concentrations, we observe the trend of declining solar cell PCEs with increasing  $R_q$ , which we discuss further in the Supporting Information (Table S1, Figure S3 and S4, Supporting Information).

### 3.2. Nano-IR

In light of earlier literature reports,<sup>[15,17,27]</sup> the assumption that the lens-shaped features observed in the PTB7:PC<sub>71</sub>BM layer topography are fullerene-rich aggregates, can be considered

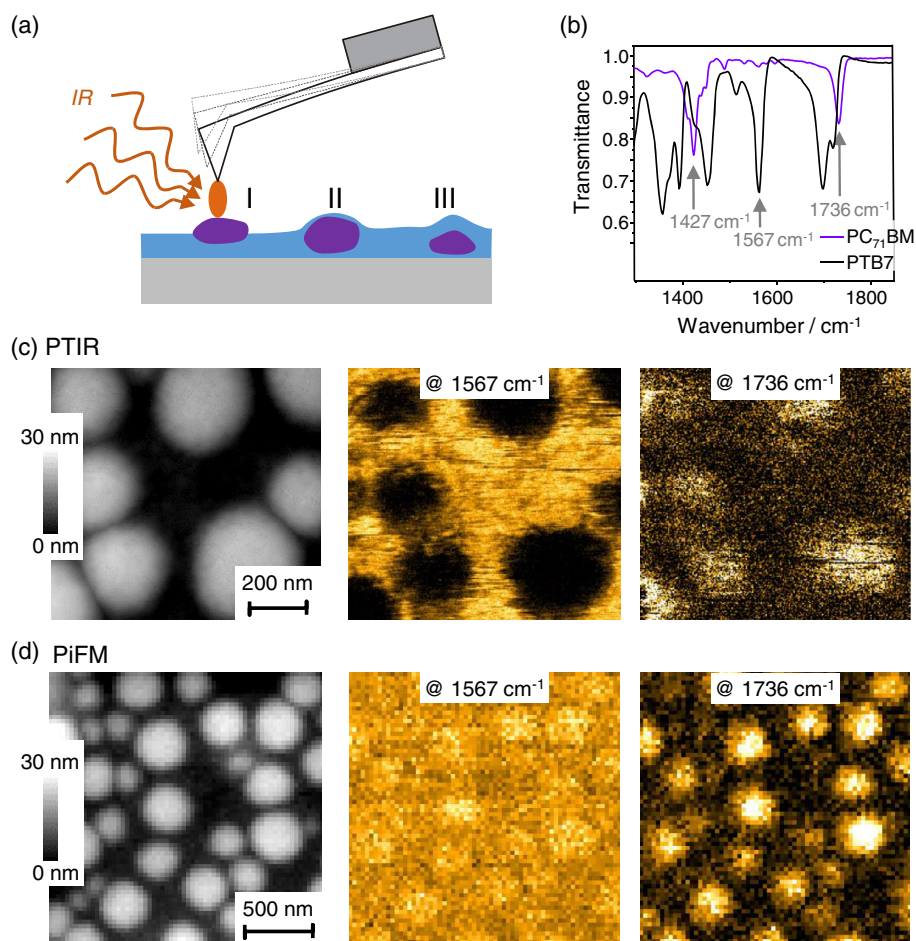


**Figure 4.** a) Nano-IR measurement principle: IR light from a quantum cascade laser is focused on the AFM tip apex region. The illustration shows three principal situations how the phases of the PTB7:PC<sub>71</sub>BM blend could be arranged in a thin-film. I: The PC<sub>71</sub>BM phase is situated at the interface to air without a skin layer; II: the PC<sub>71</sub>BM phase is covered by a skin layer of the other phase; III: the PC<sub>71</sub>BM phase is deeply buried in the thin-film. b) FT-IR spectra of PTB7 and PC<sub>71</sub>BM. c) Topography and PTIR response at 1567 and 1736 cm<sup>-1</sup> of PTB7:PC<sub>71</sub>BM samples deposited from neat *o*-xylene. d) Topography and PiFM response at 1567 and 1736 cm<sup>-1</sup> of PTB7:PC<sub>71</sub>BM samples deposited from neat *o*-xylene. Local nano-IR spectra in PTIR and PiFM mode at different positions are provided in the Supporting Information (Figure S5, Supporting Information).

rather accurate. However, their embedding into the BHJ layer remains invisible to standard AFM probing techniques. More detailed information on their nature can only be gained by correlation of surface and bulk-sensitive measurements with nanometer resolution. **Figure 4a** shows different possible aggregate configurations in the BHJ layer: 1) The fullerene aggregate protrudes from the BHJ surface. 2) The fullerene aggregate is buried in the PTB7:PC<sub>71</sub>BM layer covered with a PTB7 skin. 3) The aggregate is buried deeply in the BHJ and may or may not be visible in the layer topography.

To differentiate material phases by molecular fingerprints, we used a novel combination of infrared (IR) absorption spectroscopy and AFM, henceforth referred to as nano-IR absorption microscopy.<sup>[42–44]</sup> The measurement principle of nano-IR relies on the detection of a photothermal expansion of the sample under the tip.<sup>[42]</sup> Such photothermal expansions reach the picometer realm for a sample thickness on the order of 100 nm. Thus, measuring the photothermal expansion is sensitive into the depth of materials located under the AFM tip. As such, this

technique can be volume sensitive and is generally known as photothermal-induced resonance (PTIR) mode.

Initially, we calibrated the nanoscale measurement by analyzing the IR absorption spectra of the semiconductor powders by standard Fourier-transformed (FT)-IR spectroscopy (Figure 4b). FT-IR of neat PC<sub>71</sub>BM shows two dominant absorption peaks at 1427 cm<sup>-1</sup> (CH<sub>2</sub> bending<sup>[45]</sup>) and 1736 cm<sup>-1</sup> (C=O stretch<sup>[45]</sup>), which partially overlap with adjacent absorption peaks from neat PTB7. On the contrary, PTB7 shows several dominant FT-IR absorption peaks out of which the peak at 1567 cm<sup>-1</sup> does not overlap with PC<sub>71</sub>BM signals. Hence, we explored the sample responses under illumination at 1567 cm<sup>-1</sup> (PTB7) and 1736 cm<sup>-1</sup> (PC<sub>71</sub>BM) to distinguish both components.

Three distinctly different PTB7:PC<sub>71</sub>BM samples were then investigated, possessing medium-sized, large-sized, and no (obvious) fullerene domains:

The first PTB7:PC<sub>71</sub>BM sample was deposited from neat *o*-xylene. Figure 4c shows the recorded topography (left) and corresponding PTIR images (right) at 1567 and 1736 cm<sup>-1</sup>. At

1567  $\text{cm}^{-1}$  (PTB7), no PTIR signal was measured at the positions of the lens-shaped topographic features (black areas). However, in between the lens-shaped features a strong response was detected at this wavenumber (orange areas). At 1736  $\text{cm}^{-1}$  ( $\text{PC}_{71}\text{BM}$ ), the contrast inverses. Here, we observed a stronger PTIR response on the lens-shaped features and a weaker response in between. These PTIR measurements confirm that the lens-shaped domains indeed correspond to a  $\text{PC}_{71}\text{BM}$ -rich phase, which is embedded in a PTB7-rich phase. The absence of a PTB7 response (1567  $\text{cm}^{-1}$ ) on the lens-shaped domains allows us to exclude configuration III of the principal aggregate arrangements in the BHJ layer (Figure 4a). Nevertheless, aggregate configurations I and II would still be both feasible.

To distinguish the latter two possibilities, we operated the nano-IR in a photo-induced force microscopy (PiFM) mode: The PiFM mode uses measurements of the attractive forces arising from various photo-induced dipole–dipole forces between the absorbing sample and the metal-coated AFM tip in tapping mode configuration.<sup>[43,44,46]</sup> Being based on dipole forces, the PiFM mode is more surface sensitive. PiFM allows the resolving of the local chemical composition, e.g., the components of a semiconductor blend.<sup>[46,47]</sup> Figure 4d shows the simultaneously recorded topography (left) and PiFM images (right) at 1567  $\text{cm}^{-1}$  (PTB7) and 1736  $\text{cm}^{-1}$  ( $\text{PC}_{71}\text{BM}$ ). In PiFM mode at 1567  $\text{cm}^{-1}$  (PTB7), a more uniform response was measured regardless of topographic features. However, at 1736  $\text{cm}^{-1}$  ( $\text{PC}_{71}\text{BM}$ ), a stronger response was measured on the lens-shaped  $\text{PC}_{71}\text{BM}$  domains compared to the valley regions. The PiFM measurements at 1567  $\text{cm}^{-1}$  may also show a weak correlation with the topography as the signal of PTB7 is slightly stronger on the elevated lens-shaped features. Here, the signal is 15% larger compared with the surrounding valleys, which could indicate a slightly stronger mechanical coupling of the cantilever response at these protruding domains. Despite the possible weak crosstalk of the topography, we conclude that the entire surface is PTB7-rich and the aggregate configuration II, as shown in Figure 4a, best describes the BHJ morphology.

The second PTB7: $\text{PC}_{71}\text{BM}$  sample, which was deposited using 10% of the additive BA, showed larger and spatially further separated lens-shaped  $\text{PC}_{71}\text{BM}$  domains (Figure 5a, left image). Similar to the previous sample, the nano-IR PiFM image in Figure 5a (right side) shows a stronger response at 1736  $\text{cm}^{-1}$  ( $\text{PC}_{71}\text{BM}$ ) on the lens-shaped domains. Locally measured nano-IR spectra, recorded in PTIR mode (Figure S5, Supporting Information), clearly support the  $\text{PC}_{71}\text{BM}$ -rich composition of these lens-shaped domains as compared with the mixed valley region around, which is further discussed in the Supporting Information.

The third sample under investigation was a PTB7: $\text{PC}_{71}\text{BM}$  layer deposited from *o*-xylene with 3% AA, which produced one of the highest solar cell performances in this study. Those samples are not peculiar in topography (Figure 5b, left image). The insets in Figure 5b show the topography and the PiFM image at higher magnification. Only on a scale <100 nm, we observed a modulation of the  $\text{PC}_{71}\text{BM}$  density at 1736  $\text{cm}^{-1}$ . Here,  $\text{PC}_{71}\text{BM}$ -rich domains with diameters between 50 and 80 nm are visible. These domains are either present at the surface or are coated with an ultrathin PTB7 layer, which cannot be resolved with nano-IR.

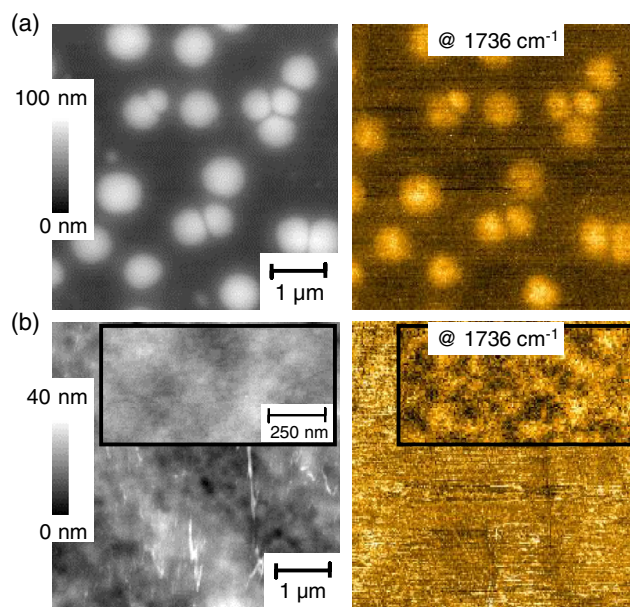


**Figure 5.** a) Topography and PiFM response of PTB7: $\text{PC}_{71}\text{BM}$  samples processed using 10% BA additive. b) Topography and PiFM response of PTB7: $\text{PC}_{71}\text{BM}$  samples processed using 3% AA. The inset shows the topography and PiFM response at higher magnification. Here, the topography gray scale ranges from 0 to 20 nm. Local nano-IR spectra in PTIR and PiFM modes at different positions are provided in the Supporting Information (Figure S5, Supporting Information).

Altogether, the nano-IR combination of the two modes (PTIR and PiFM) is a powerful tool to analyze the subsurface and surface micromorphology of the PTB7: $\text{PC}_{71}\text{BM}$  blend. The results discussed herein based on nano-IR imaging at specific wavenumbers are supported by additional nano-IR spectra that were measured locally on representative sample positions (Figure S5, Supporting Information). Only the combination of both nano-IR modes allowed us to conclude that the lens-shaped  $\text{PC}_{71}\text{BM}$  domains are covered by a PTB7-rich skin layer. The valleys around the lens-shaped  $\text{PC}_{71}\text{BM}$  domains are PTB7-rich. The size of the  $\text{PC}_{71}\text{BM}$  domains is determined by the type and concentration of the additive. Although the layers processed from *o*-xylene and 3% AA exhibit a vastly featureless topography, PTIR and PiFM identified  $\text{PC}_{71}\text{BM}$ -rich domains with dimensions of about 50 nm. As the latter solvent combination produced the highest solar cell PCE, we conclude that  $\text{PC}_{71}\text{BM}$  aggregates of this size are not detrimental to efficient charge carrier generation and transport.

### 3.3. STEM

To support the AFM and the nano-IR analysis, we carried out STEM imaging of cross-sectional lamellae that were prepared from different PTB7: $\text{PC}_{71}\text{BM}$  layers using a focused-ion-beam. In contrast to the scanning force methods, this approach provides direct access to the bulk of the sample. Figure 6 shows 30 keV bright field (BF) STEM cross-sectional images of the PTB7: $\text{PC}_{71}\text{BM}$  lamellae (thickness: 150–170 nm). As the

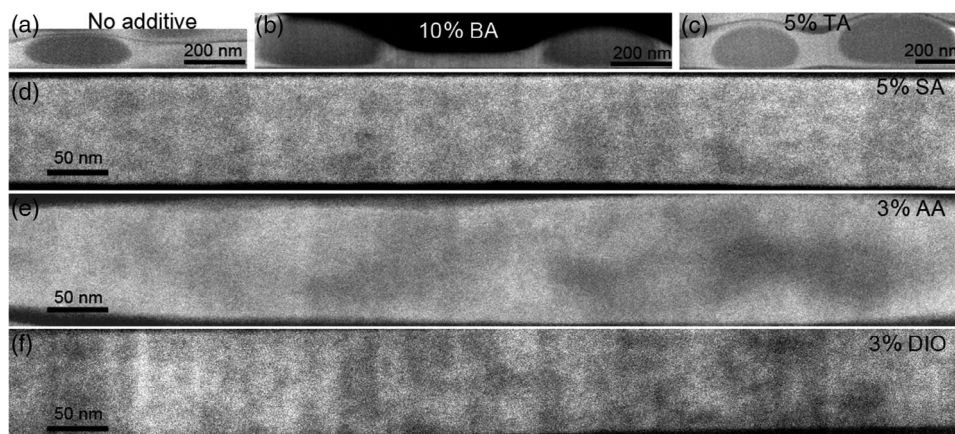


**Figure 6.** BF-STEM images of cross-sectional lamellae of PTB7:PC<sub>71</sub>BM layers processed with different additives. a) No additive, b) 10% BA, c) 5% TA, d) 5% SA, e) 3% AA, and f) 3% DIO. The darker PC<sub>71</sub>BM-rich domains are clearly visible in the blends processed without solvent additive or either of the poor solvent additives (BA, TA). A PTB7-rich cover layer is clearly visible in (c), whereas it is partially concealed by the Pt-protection layer in (b). We note that, in (a) and (c), multiple layers were stacked before lamella cutting for better specimen stability, thin dark lines mark residual PEDOT:PSS interfaces between layers. Cross sections of layers processed with 5% SA, 3% AA, and 3% DIO do not show large-scale phase separation but PTB7- and PC<sub>71</sub>BM-rich regions with sizes on the order of a few ten nanometers.

preparation of the lamellae produced specimens with homogeneous thicknesses, the two materials with different electron scattering properties can be distinguished by the BF-STEM intensity. However, the contrast of PTB7 and PC<sub>71</sub>BM is not obvious due to the small difference in average atomic number and material density, which mainly determine electron scattering. To correlate the semiconductors with the bright and dark regions in the BF-STEM image, we simulated the BF-STEM intensities of neat PTB7 and PC<sub>71</sub>BM at a primary electron energy of 30 keV, which is further discussed in the Supporting Information (Figure S6, Supporting Information). The simulations show that PC<sub>71</sub>BM phases appear darker than PTB7 phases.

The BF-STEM cross-sectional images of lamellae prepared from layers processed from neat *o*-xylene, *o*-xylene:BA (10% BA) and *o*-xylene:TA (5% TA) are shown in Figure 6a–c. Macro-phase separation into a structure comprising PC<sub>71</sub>BM-rich domains in a polymer-rich environment is consistent with the observations by PiFM and PTIR and, in particular, the formation of the 5–30 nm-thick PTB7-rich skin layer. The average size of the PC<sub>71</sub>BM-rich domains in the BA- and TA-processed samples exceeds the size of the domains in the additive-free sample, which agrees with the outcome of the AFM topography analysis. Interestingly, the cross-sectional images of PTB7:PC<sub>71</sub>BM blends also show PC<sub>71</sub>BM-rich domains in the regions with depressed topography (e.g., when processed with 1% DIO), which is an unforeseen outcome of our analysis and which we further discuss in the Supporting Information (Figure S7, Supporting Information).

In contrast, macro-phase separated domains were not observed upon using either of the other three additives (SA, AA, and DIO) at the concentrations that provided optimal device performance. In the corresponding Figure 6d–f, BF-STEM intensity modulations are visible on a smaller scale compared with Figure 6a–c. The sample processed with 3% AA shows PC<sub>71</sub>BM-rich domains with lateral sizes between 50 and 200 nm, whereas PTB7:PC<sub>71</sub>BM blends processed with 5% SA

and 3% DIO contain even smaller domains on the order of a few ten nanometers. PC<sub>71</sub>BM-rich domains in the sample processed with 3% AA can be of similar size as in the additive-free sample (Figure 6a). However, PC<sub>71</sub>BM-rich domains in the latter sample are condensed and spatially separated while they are interconnected in the 3% AA sample which is again consistent with the nano-IR measurements.

Domain interconnectivity and small-scale phase separation on the order of the exciton diffusion length of some 10 nm make losses from inefficient exciton dissociation and charge carrier transport less likely, explaining the high  $J_{SC}$  and FF measured in the devices based on 3% AA, 5% SA, and 3% DIO-processed BHJ blends.

#### 4. Solubility in Solvent Additives

The morphological analysis produced a comprehensive picture of the BHJ micromorphology in dependence of the solvent additive (and concentration) used during processing. The remaining question is why the structurally similar solvent additives have different effects on the BHJ formation.

In light of earlier reports which investigated the solubility of the BHJ compounds, we quantified the solubility of PTB7 and PC<sub>71</sub>BM in the various solvent additives, following established protocols.<sup>[48,49]</sup> Figure 7 and Table 2 show the solubility of PC<sub>71</sub>BM and PTB7 in the different solvent additives and, for comparison, in the main solvent *o*-xylene. PC<sub>71</sub>BM dissolves well in *o*-xylene at a concentration > 30 mg mL<sup>-1</sup> at room temperature. It also dissolves at a concentration > 30 mg mL<sup>-1</sup> in SA and DIO. In BA, TA, and AA, the solubility of PC<sub>71</sub>BM is 17.5, 22.8, and 16.7 mg mL<sup>-1</sup>, respectively. At room temperature, PTB7 dissolves in *o*-xylene at 18.5 mg mL<sup>-1</sup>. The solubility of PTB7 in TA is 0.015 mg mL<sup>-1</sup>, whereas the solubility in all other solvent additives is too small to be accurately determined. We estimate these solubility limits to be on the order of 0.005 mg mL<sup>-1</sup>.



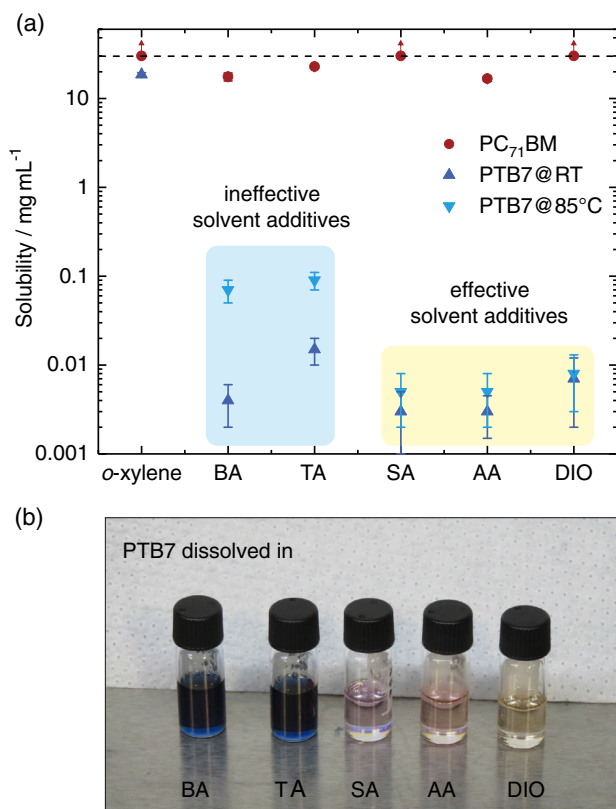


**Figure 7.** a) Solubility of PC<sub>71</sub>BM and PTB7 in the main solvent *o*-xylene and the different solvent additives at room temperature. In addition, the solubility of PTB7 at 85 °C is depicted. The PTB7 solubility difference of one order of magnitude at 85 °C correlates with the effectiveness of the solvent additives for optimized device performance. b) Photograph of PTB7 dissolved in the solvent additives at 85 °C after 2 days and filtration.

**Table 2.** Solubilities of PC<sub>71</sub>BM and PTB7 in the main solvent *o*-xylene and the solvent additives.

| Solvent          | bp <sup>a)</sup> [°C] | p <sup>b)</sup> [mbar]    | Solubility [mg mL <sup>-1</sup> ] |               |                 |
|------------------|-----------------------|---------------------------|-----------------------------------|---------------|-----------------|
|                  |                       |                           | PC <sub>71</sub> BM               | PTB7          | PTB7 (85 °C)    |
| <i>o</i> -xylene | 144                   | 8.82                      | >30                               | 18.5 ± 1.0    | – <sup>c)</sup> |
| BA               | 179                   | 1.69                      | 17.5 ± 1.8                        | 0.004 ± 0.002 | 0.07 ± 0.02     |
| TA               | 204                   | 0.33                      | 22.8 ± 1.0                        | 0.015 ± 0.005 | 0.09 ± 0.02     |
| SA               | 197                   | 0.79                      | >30                               | 0.003 ± 0.002 | 0.005 ± 0.003   |
| AA               | 250                   | 2.85 × 10 <sup>-2</sup>   | 16.7 ± 1.1                        | 0.003 ± 0.002 | 0.005 ± 0.003   |
| DIO              | 333 <sup>d)</sup>     | 3.75 × 10 <sup>-4d)</sup> | >30                               | 0.007 ± 0.005 | 0.008 ± 0.005   |

<sup>a)</sup>Boiling point at 1 atm; <sup>b)</sup>vapor pressure at 25 °C from the European Chemicals Agency database at [www.echa.europa.eu](http://www.echa.europa.eu); <sup>c)</sup>not determined; <sup>d)</sup>from the database at [www.molbase.com](http://www.molbase.com).

As the blend solution is usually processed at elevated temperatures, we repeated the solubility study at 85 °C. As the inherent cooling during centrifugation would corrupt these measurement results, in this experiment, we opted for filtering to remove large aggregates instead. Figure 7b shows a photo of the 85 °C warm

PTB7 supernatant after filtering, clearly demonstrating the higher solubility of PTB7 in BA and TA versus SA, AA, and DIO. In SA, AA, and DIO, the solubility below 0.01 mg mL<sup>-1</sup> was effectively not enhanced in comparison with room temperature, but we found an enhanced solubility of 0.07 mg mL<sup>-1</sup> in BA and of 0.09 mg mL<sup>-1</sup> in TA, which is an order of magnitude higher than the PTB7 solubility in all other solvent additives.

This correlates with the observation that BA and TA differ significantly in their impact on the morphology from SA, AA, or DIO. Processing with BA or TA led to macro-phase separation at all concentrations and hardly improved device performance as compared with solar cells processed omitting all additives. In contrast, processing using an optimal concentration of SA, AA, and DIO effectively suppressed macro-phase separation and reduced the size of fullerene-rich domains to the nanoscale.

The fullerene solubility >15 mg mL<sup>-1</sup> in all solvent additives is about 3 orders of magnitude higher than the corresponding polymer solubility. Therefore, we conclude that the lowest solubility of the polymer in this series of substituted benzaldehydes is decisive for rendering the solvent additive effective. Even though any thermodynamic solubility limit can, at its best, only hint at the results of the kinetic processes during film solidification, we interpret our result according to the following mechanism<sup>[18]</sup>: During thin-film formation, a solvent additive, in which the polymer shows lowest solubility (here: SA, AA, and DIO), will induce earlier aggregation and thus increase solution viscosity, reduce the mobility for L–L demixing and reduce the time for separated liquid phases to grow.

In contrast, solvent additives which accommodate the polymer well are not effective in suppressing macro-phase separation (BA and TA), and allow the coarsening (coalescence and ripening) to increase the feature size of phase separated PC<sub>71</sub>BM domains, due to a prolonged drying time. Interestingly, in this series of substituted benzaldehydes, the volatility of the solvent additives appears to not play a major role: Although TA and SA possess very similar boiling points of about 200 °C and vapor pressures (Table 2), only the latter is an effective solvent additive. Similarly, we observed that AA and DIO did not produce more efficient solar cells than SA, despite significantly higher boiling points and longer drying times. All three solvent additives produced the same optimum solar cell performance (PCE = 7%).

## 5. Conclusion

We have investigated a series of substituted benzaldehydes as processing additives for the fabrication of PTB7:PC<sub>71</sub>BM BHJs from *o*-xylene solution. When deposited from neat *o*-xylene solution, PTB7 and PC<sub>71</sub>BM are prone to L–L demixing, producing solar cells with low performance. The addition of AA, SA, or the reference additive DIO to the *o*-xylene solution effectively suppresses L–L demixing for optimized BJJ morphologies and solar cell performance, whereas BA and TA have only little to no positive effect. We find the most dominant difference in the one order of magnitude higher solubility of the polymer in BA and TA as compared with SA, AA, and DIO. This agrees with our understanding of the BJJ formation that, upon evaporation of the main solvent *o*-xylene, the polymer solubility must be

reduced to trigger an immediate solidification of the polymer matrix, hence suppressing L–L demixing and disabling the aggregation of fullerenes.

Earlier works reported that, for a controlled phase separation of BHJs that mix too intimately (such as PCPDTBT:PC<sub>71</sub>BM), additives with high fullerene solubility (i.e., selectivity) are required, which allows the two semiconductor phases to aggregate and to form charge carrier pathways to the electrodes.<sup>[33]</sup> From this experimental work, we conclude that the suppression of too strong phase separation in BHJs requires not only good solubility of the fullerene but also lowest solubility of the polymer in the additive. While earlier works have proposed high fullerene solubility, we found that this requirement is insufficient. In our exemplary PTB7:PC<sub>71</sub>BM blend, the solvent additive must also provide selective nonsolubility of the polymer to achieve optimal device performance. Even the smallest polymer solubility can render the additive unsuitable for producing high solar cell performance.

The previous classification of solvent additives into aromatic or non-aromatic,<sup>[50,51]</sup> based on different operating mechanisms for representatives of each category, such as ODT versus CN,<sup>[34,35]</sup> also appears insufficient. Effective aromatic substituted benzaldehydes act via aggregation due to poor polymer solubility and are therefore different from aromatic solvent additives with rather good polymer solubility, operating via prolonged drying.<sup>[35]</sup> Notably, SA and AA exhibit neither extremely low volatility nor an extremely high fullerene solubility of more than 100 mg mL<sup>-1</sup>, both of which were reported previously to be important properties of the solvent additives CN, DPE, or DIO.<sup>[19,29,52,53]</sup>

In our earlier work on the principal applicability of AA as solvent additive for the formation of highly efficient BHJs, we demonstrated the broad usability of AA on a range of polymer:fullerene combinations.<sup>[39]</sup> In light of this previous work and many other reports on the use of AA for different BHJs,<sup>[40,54,55]</sup> we infer that the mechanistic description of BHJ formation upon implementation of either of the four benzaldehyde additives SA, AA, TA, and BA in this work can be translated also to other polymer:fullerene systems.

## 6. Experimental Section

**Organic Solar Cell Fabrication:** Devices were fabricated according to a glass/ITO/ZnO/photoactive layer/MoO<sub>x</sub>/Ag device architecture as shown in the inset of Figure 2a. Patterned ITO-coated glass substrates (125 nm, 15 Ω<sub>□</sub>) were cleaned by sequential ultrasonication in acetone and 2-propanol (10 min) and afterward transferred into a nitrogen glovebox for further fabrication and characterization. A ZnO electron extraction layer was spun from nanoparticle dispersion (Avantama, 1 wt% in 2-propanol, 4000 rpm, 30 s, 30 nm) and thermally annealed on a hotplate (80 °C, 10 min). Poly[[4,8-bis[(2-ethylhexyl)oxy]benzo[1,2-b:4,5-b']dithiophene-2,6-diyl] [3-fluoro-2-[(2-ethylhexyl)carbonyl]thieno[3,4-b]thiophenediyl]] (PTB7, 1-Material Inc., M<sub>w</sub> = 131 kg mol<sup>-1</sup>, D<sub>M</sub> = 2.5) and [6,6]-phenyl C<sub>71</sub>-butyric acid methyl ester (PC<sub>71</sub>BM, Solenne, 99%) were dissolved (1:1.5 w/w, total concentration 25 mg mL<sup>-1</sup>) in *o*-xylene (Sigma-Aldrich, anhydrous, 97%) at 85 °C overnight. Then, either of the solvent additives benzaldehyde (BA, Sigma-Aldrich, ≥99.5%), *p*-tolualdehyde (TA, Acros Organics, 99+%), SA (Acros Organics, 99%), *p*-anisaldehyde (AA, Sigma-Aldrich, 98%) or DIO (Alfa Aesar, stabilized with copper, 98%) was added in relation to the main solvent volume (e.g., 1 mL of main solvent plus 10 μL of additive is denoted as an additive concentration of 1%). The photoactive layer was

spin cast (1500 rpm, 60 s, 90 nm) from warm (85 °C) solution onto the samples and dried at room temperature. Only in the case of DIO, an additional drying step was applied at elevated temperature (50 °C, 20 min) on the next day to remove residues before evaporation of the top electrode. Then the devices were transferred into a vacuum chamber (base pressure 10<sup>-6</sup> mbar) to thermally evaporate a MoO<sub>x</sub> charge carrier transport layer (10 nm) and the Ag top electrode (100 nm) using a shadow mask to set the photoactive area of the solar cell to 0.105 cm<sup>2</sup>. All solvents were stored in nitrogen atmosphere and used as received.

**Device Characterization:** For the optoelectronic characterization, the solar cells were exposed to artificial sunlight (Oriel VeraSol-2 LED Class AAA) corresponding to the solar spectrum (ASTM AM 1.5G, 1000 W m<sup>-2</sup>), calibrated by a KG5-filtered silicon reference cell (91150-KG5, Newport). Current density–voltage (*J*–*V*) curves were recorded with a source-measurement unit (Keithley 2450). Before the measurements, the solar cells were exposed to UV-A light (365 nm, Opsytec Dr. Gröbel, UV hand-held lamp, 6 W, 10 min). Layer thicknesses were measured with a tactile stylus profiler (Dektak XT, Bruker).

**AFM Topography:** AFM images of the light-harvesting layer of fully functional solar cells were recorded next to the top electrodes in PeakForce Tapping mode (Dimension ICON, Bruker, RTESPA tip). For a quantitative analysis (NanoScope Analysis, Bruker), all images were corrected by a first-order plane fit using a height exclusion threshold such that any protruding lens-shaped domains did not affect the plane fit. Thereby, zero height was set to the maximum of the height distribution. Average diameters and protrusion heights of the fullerene domains were determined by the particle analysis function and are shown in Table S1, Supporting Information.

**Nano-IR:** Nano-IR microscopy (VistaScope, MolecularVista,) was carried out in PiFM and PTIR mode.<sup>[42–44]</sup> For PiFM, the second eigenmode of the cantilever resonance frequency was used for the topography feedback. The first eigenmode was then used to pick up IR light-induced forces. The IR light was modulated at the difference frequency between the first and second eigenmodes (sideband configuration). This difference frequency was fine-tuned while the tip was engaged on the surface. For displaying the local IR response, we recorded the cantilever amplitude at the frequency of the first eigenmode. For PTIR, we recorded the topography in contact mode while modulating the incident IR intensity at a higher eigenmode of the cantilever resonance frequency. For PiFM and PTIR, we used the same cantilever (NCH-PiFM-CF or SD-FMAu25). Local nano-IR spectra were recorded in PiFM and PTIR mode. Spectra in either PiFM or PTIR mode were recorded by ramping the wavenumber of the IR light from 850 to 1850 cm<sup>-1</sup>. One spectrum was typically recorded within 20–30 s. Samples for measuring nano-IR images were prepared on cleaned glass substrates, identical to the light-harvesting thin-films in solar cells.

**STEM:** Thin cross-sectional lamellae of BHJ layers were prepared via focused Ga-ion-beam milling in a dual beam instrument (ThermoFisher Helios G4 FX), which is equipped with a double-tilt specimen holder for electron-transparent samples and a 16-bit multisegmented silicon STEM detector. First, the PTB7:PC<sub>71</sub>BM layers (fabricated as described earlier) were deposited on poly(3,4-ethylenedioxythiophene):polystyrene sulfonate (PEDOT:PSS) sacrificial layers atop cleaned glass substrates. For this purpose, we diluted PEDOT:PSS (Clevios P VP Al 4083) with ethanol (1:1 by volume), spin cast a thin-film (4000 rpm, 30 s, 60 nm) and annealed the sample (120 °C, 10 min). Then, the BHJ layers were floated off in water and picked up by a silicon wafer. For better handling and cross-sectional imaging, multiple blend layers were stacked as described in more detail in the study by Li et al.<sup>[56]</sup> Two consecutive protective layers of 1 μm of electron-beam-deposited Pt and 1 μm of ion-beam-deposited Pt were used to avoid damage due to Ga-ion implantation during milling. A cross-sectional lamella was extracted from this bulk sample and attached to a Cu support grid. Final milling to electron transparency was carried out by reducing the Ga-ion energy from 30 keV to 5 kV with a low ion current of 12 pA. The PTB7:PC<sub>71</sub>BM morphology was characterized in BF-STEM mode at a primary electron energy of 30 keV. The simulations of the normalized BF-STEM intensity as a function of thickness of neat PTB7 or PC<sub>71</sub>BM were performed with the NISTMonte package using Screened Rutherford cross sections.<sup>[57]</sup>

**Solubility Investigation:** PC<sub>71</sub>BM and PTB7 were dissolved (30 mg mL<sup>-1</sup>) in the solvents and shaken (2 days, room temperature). Afterward, the (saturated) solutions were transferred to tubes (Eppendorf Safe-Lock, 1.5 mL) and centrifuged (MiniSpin Plus, Eppendorf, 14 500 rpm, 10 min). The supernatant was diluted and filled into quartz cuvettes, and the UV–vis absorbance was measured (Cary5000, Agilent). The absorbance was then compared with the linear relation between concentration and absorbance, determined previously based on dilute solutions with known concentrations of PC<sub>71</sub>BM or PTB7 in *o*-xylene. For the determination of the solubility of PTB7 in the solvent additives at elevated temperature, solutions were heated (2 days, 85 °C), filtered (PTFE, 0.2 μm), diluted and analyzed identically by UV–vis absorbance.

## Supporting Information

Supporting Information is available from the Wiley Online Library or from the author.

## Acknowledgements

This work was supported by the European Commission through the project MatHero, funded within the European Union's Seventh Framework Programme for research, technological development and demonstration under grant agreement no. 604603. The AFM was made available through funding by the Federal Ministry of Education and Research (Project TAURUS, grant no. 03EK3504). The authors thank Avantama Ltd. for supplying zinc oxide nanoparticles. The authors thank Helma Burg (MPI-P) for supporting the nano-IR measurements. In addition, the authors thank Dr. Anne Müller from Anfatec and Dr. Derek Novak from Molecular Vista for the discussion of the nano-IR results.

Open access funding enabled and organized by Projekt DEAL.

## Conflict of Interest

The authors declare no conflict of interest.

## Data Availability Statement

The data that support the findings of this study are available from the corresponding author upon reasonable request.

## Keywords

bulk heterojunctions, morphologies, organic photovoltaics, phase separation, solvent additives

Received: March 31, 2021

Revised: June 8, 2021

Published online:

- [1] S. Berny, N. Blouin, A. Distler, H.-J. Egelhaaf, M. Krompiec, A. Lohr, O. R. Lozman, G. E. Morse, L. Nanson, A. Pron, T. Sauermann, N. Seidler, S. Tierney, P. Tiwana, M. Wagner, H. Wilson, *Adv. Sci.* **2016**, *3*, 1500342.
- [2] D. Landerer, D. Bahro, H. Röhme, M. Koppitz, A. Mertens, F. Manger, F. Denk, M. Heindinger, T. Windmann, A. Colsmann, *Energy Technol.* **2017**, *5*, 1936.
- [3] R. Garcia-Valverde, J. A. Villarejo, M. Hösel, M. V. Madsen, R. R. Søndergaard, M. Jørgensen, F. C. Krebs, *Sol. Energy Mater. Sol. Cells* **2016**, *144*, 48.

- [4] A. Colsmann, H. Röhme, C. Sprau, *Sol. RRL* **2020**, *4*, 2000015.
- [5] Y. Lin, B. Adilbekova, Y. Firdaus, E. Yengel, H. Faber, M. Sajjad, X. Zheng, E. Yarali, A. Seitkhan, O. M. Bakr, A. El-Labban, U. Schwingenschlög, V. Tung, I. McCulloch, F. Laquai, T. D. Anthopoulos, *Adv. Mater.* **2019**, *31*, 1902965.
- [6] Y. Cui, H. Yao, J. Zhang, K. Xian, T. Zhang, L. Hong, Y. Wang, Y. Xu, K. Ma, C. An, C. He, Z. Wei, F. Gao, J. Hou, *Adv. Mater.* **2020**, *32*, 1908205.
- [7] Q. Liu, Y. Jiang, K. Jin, J. Qin, J. Xu, W. Li, J. Xiong, J. Liu, Z. Xiao, K. Sun, S. Yang, X. Zhang, L. Ding, *Sci. Bull.* **2020**, *65*, 272.
- [8] L. Arunagiri, Z. Peng, X. Zou, H. Yu, G. Zhang, Z. Wang, J. Y. Lin Lai, J. Zhang, Y. Zheng, C. Cui, F. Huang, Y. Zou, K. S. Wong, P. C. Y. Chow, H. Ade, H. Yan, *Joule* **2020**, *4*, 1.
- [9] R. Xue, J. Zhang, Y. Li, Y. Li, *Small* **2018**, *14*, 1801793.
- [10] F. Padinger, R. S. Rittberger, N. S. Sariciftci, *Adv. Funct. Mater.* **2003**, *13*, 85.
- [11] G. Li, V. Shrotriya, J. Huang, Y. Yao, T. Moriarty, K. Emery, Y. Yang, *Nat. Mater.* **2005**, *4*, 864.
- [12] G. Li, Y. Yao, H. Yang, V. Shrotriya, G. Yang, Y. Yang, *Adv. Funct. Mater.* **2007**, *17*, 1636.
- [13] J. H. Park, J. S. Kim, J. H. Lee, W. H. Lee, K. Cho, *J. Phys. Chem. C* **2009**, *113*, 17579.
- [14] S. Kouijzer, J. J. Michels, M. van den Berg, V. S. Gevaerts, M. Turbiez, M. M. Wienk, R. A. J. Janssen, *J. Am. Chem. Soc.* **2013**, *135*, 12057.
- [15] Y. Liang, Z. Xu, J. Xia, S.-T. Tsai, Y. Wu, G. Li, C. Ray, L. Yu, *Adv. Mater.* **2010**, *22*, E135.
- [16] C. M. Amb, S. Chen, K. R. Graham, J. Subbiah, C. E. Small, F. So, J. R. Reynolds, *J. Am. Chem. Soc.* **2011**, *133*, 10062.
- [17] B. A. Collins, Z. Li, J. R. Tumbleston, E. Gann, C. R. McNeill, H. Ade, *Adv. Energy Mater.* **2013**, *3*, 65.
- [18] J. J. van Franeker, M. Turbiez, W. Li, M. M. Wienk, R. A. J. Janssen, *Nat. Commun.* **2015**, *6*, 6229.
- [19] D. Liu, Z. Wang, S. Zhang, Z. Zheng, B. Yang, W. Ma, J. Hou, *RSC Adv.* **2015**, *5*, 69567.
- [20] W. Zhao, L. Ye, S. Zhang, M. Sun, J. Hou, *J. Mater. Chem. A* **2015**, *3*, 12723.
- [21] D. Bartesaghi, M. Turbiez, L. J. A. Koster, *Org. Electron.* **2014**, *15*, 3191.
- [22] J. Kniepert, I. Lange, J. Heidbrink, J. Kurpiers, T. J. K. Brenner, L. J. A. Koster, D. Neher, *J. Phys. Chem. C* **2015**, *119*, 8310.
- [23] M. M. Wienk, M. Turbiez, J. Gilot, R. A. J. Janssen, *Adv. Mater.* **2008**, *20*, 2556.
- [24] D. H. Wang, P. Morin, C. Lee, A. K. Ko Kyaw, M. Leclerc, A. J. Heeger, *J. Mater. Chem. A* **2014**, *2*, 15052.
- [25] A. Zusan, B. Gieseking, M. Zerson, V. Dyakonov, R. Magerle, C. Deibel, *Sci. Rep.* **2015**, *5*, 8286.
- [26] X. Fan, J. Wang, H. Huang, H. Wang, *ACS Photonics* **2014**, *1*, 1278.
- [27] F. Liu, W. Zhao, J. R. Tumbleston, C. Wang, Y. Gu, D. Wang, A. L. Briseno, H. Ade, T. P. Russell, *Adv. Energy Mater.* **2014**, *4*, 1301377.
- [28] F.-C. Chen, H.-C. Tseng, C.-J. Ko, *Appl. Phys. Lett.* **2008**, *92*, 103316.
- [29] C. V. Hoven, X.-D. Dang, R. C. Coffin, J. Peet, T.-Q. Nguyen, G. C. Bazan, *Adv. Mater.* **2010**, *22*, E63.
- [30] J. Peet, J. Y. Kim, N. E. Coates, W. L. Ma, D. Moses, A. J. Heeger, G. C. Bazan, *Nat. Mater.* **2007**, *6*, 497.
- [31] T. L. Nguyen, H. Choi, S.-J. Ko, M. A. Uddin, B. Walker, S. Yum, J.-E. Jeong, M. H. Yun, T. J. Shin, S. Hwang, J. Y. Kim, H. Y. Woo, *Energy Environ. Sci.* **2014**, *7*, 3040.
- [32] H. Choi, S.-J. Ko, T. Kim, P.-O. Morin, B. Walker, B. H. Lee, M. Leclerc, J. Y. Kim, A. J. Heeger, *Adv. Mater.* **2015**, *27*, 3318.

- [33] J. K. Lee, W. L. Ma, C. J. Brabec, J. Yuen, J. S. Moon, J. Y. Kim, K. Lee, G. C. Bazan, A. J. Heeger, *J. Am. Chem. Soc.* **2008**, *130*, 3619.
- [34] N. Shin, L. J. Richter, A. a. Herzog, R. J. Kline, D. M. DeLongchamp, *Adv. Energy Mater.* **2013**, *3*, 938.
- [35] L. J. Richter, D. M. DeLongchamp, F. A. Bokel, S. Engmann, K. W. Chou, A. Amassian, E. Schaible, A. Hexemer, *Adv. Energy Mater.* **2015**, *5*, 1400975.
- [36] C. McDowell, G. C. Bazan, *Curr. Opin. Green Sustain. Chem.* **2017**, *5*, 49.
- [37] J. Cho, S. H. Yu, D. S. Chung, *J. Mater. Chem. C* **2017**, *5*, 2745.
- [38] S. Zhang, L. Ye, H. Zhang, J. Hou, *Mater. Today* **2016**, *19*, 533.
- [39] C. Sprau, F. Buss, M. Wagner, D. Landerer, M. Koppitz, A. Schulz, D. Bahro, W. Schabel, P. Scharfer, A. Colsmann, *Energy Environ. Sci.* **2015**, *8*, 2744.
- [40] J. Czolk, D. Landerer, M. Koppitz, D. Nass, A. Colsmann, *Adv. Mater. Technol.* **2016**, *1*, 1600184.
- [41] C. H. Y. Ho, Q. Dong, H. Yin, W. W. K. Leung, Q. Yang, H. K. H. Lee, S. W. Tsang, S. K. So, *Adv. Mater. Interfaces* **2015**, *2*, 1500166.
- [42] A. Dazzi, R. Prazeres, F. Glotin, J. M. Ortega, *Opt. Lett.* **2005**, *30*, 2388.
- [43] D. Nowak, W. Morrison, H. K. Wickramasinghe, J. Jahng, E. Potma, L. Wan, R. Ruiz, T. R. Albrecht, K. Schmidt, J. Frommer, D. P. Sanders, S. Park, *Sci. Adv.* **2016**, *2*, e1501571.
- [44] R. A. Murdick, W. Morrison, D. Nowak, T. R. Albrecht, J. Jahng, S. Park, *Jpn. J. Appl. Phys.* **2017**, *56*, 08LA04.
- [45] G. Kalonga, *J. Chem. Eng. Mater. Sci.* **2013**, *4*, 93.
- [46] X. Liu, C. Zhang, C. Duan, M. Li, Z. Hu, J. Wang, F. Liu, N. Li, C. J. Brabec, R. A. J. Janssen, G. C. Bazan, F. Huang, Y. Cao, *J. Am. Chem. Soc.* **2018**, *140*, 8934.
- [47] C. Sun, F. Pan, H. Bin, J. Zhang, L. Xue, B. Qiu, Z. Wei, Z.-G. Zhang, Y. Li, *Nat. Commun.* **2018**, *9*, 743.
- [48] K. R. Graham, P. M. Wieruszewski, R. Stalder, M. J. Hartel, J. Mei, F. So, J. R. Reynolds, *Adv. Funct. Mater.* **2012**, *22*, 4801.
- [49] F. Machui, S. Langner, X. Zhu, S. Abbott, C. J. Brabec, *Sol. Energy Mater. Sol. Cells* **2012**, *100*, 138.
- [50] Y. Choi, G. Kim, H. Kim, S. H. Lee, S. Kwon, J. Kim, K. Lee, *Nano Energy* **2016**, *30*, 200.
- [51] S. Kwon, H. Kang, J.-H. Lee, J. Lee, S. Hong, H. Kim, K. Lee, *Adv. Energy Mater.* **2017**, *7*, 1601496.
- [52] X. Cao, M. Li, J. Liu, H. Wang, K. Zhou, Y. Han, *Org. Electron.* **2015**, *24*, 280.
- [53] F. Machui, P. Maisch, I. Burgués-Ceballos, S. Langner, J. Krantz, T. Ameri, C. J. Brabec, *ChemPhysChem* **2015**, *16*, 1275.
- [54] P. Li, M. Mainville, Y. Zhang, M. Leclerc, B. Sun, R. Izquierdo, D. Ma, *Small* **2019**, *15*, 1804671.
- [55] M. E. Farahat, A. Laventure, M. A. Anderson, M. Mainville, F. Tintori, M. Leclerc, E. L. Ratcliff, G. C. Welch, *ACS Appl. Mater. Interfaces* **2020**, *12*, 43684.
- [56] Y. Li, E. Müller, C. Sprau, A. Colsmann, D. Gerthsen, *Adv. Struct. Chem. Imaging* **2020**, *6*, 2.
- [57] N. W. M. Ritchie, *Surf. Interface Anal.* **2005**, *37*, 1006.